

INFRARED VIEWS OF THE TW HYDRA DISK

A. J. WEINBERGER,^{1,2} E. E. BECKLIN,¹ G. SCHNEIDER,³ E. I. CHIANG,⁴ P. J. LOWRANCE,^{1,5} M. SILVERSTONE,³
B. ZUCKERMAN,¹ D. C. HINES,³ AND B. A. SMITH⁶

Received 2001 April 11; accepted 2001 October 15

ABSTRACT

The face-on disk around TW Hya is imaged in scattered light at 1.1 and 1.6 μm using the coronagraph in the Near Infrared Camera and Multi Object Spectrometer aboard the *Hubble Space Telescope*. Stellar light scattered from the optically thick dust disk is seen from 20 to 230 AU. The surface brightness declines as a power law of $r^{-2.6 \pm 0.1}$ between 45 and 150 AU. The scattering profile indicates that the disk is flared, not geometrically flat. The disk, while spatially unresolved in thermal radiation at 12 and 18 μm in observations from the W. M. Keck Observatory, shows amorphous and crystalline silicate emission in its spectrum. A disk with silicate grains of a radius $\sim 1 \mu\text{m}$ in size in its surface layers can explain the color of the scattered light and the shape of the mid-infrared spectrum. Much larger grains in the disk interior are necessary to fit the millimeter-wave spectral energy distribution, and hence grain growth from an original interstellar size population may have occurred.

Subject headings: circumstellar matter — infrared: stars — stars: individual (TW Hya)

1. INTRODUCTION

TW Hya (= CD $-34^\circ 7151$, $H = 7.6$ mag) is a star with a large H α -emission equivalent width, visual variability, and location at 23° Galactic latitude, and it was thus labeled as “peculiar” by Henize (1976). Rucinski & Krautter (1983) identified it as a spectral type K7 Ve T Tauri star far from any molecular cloud (i.e., “isolated”). TW Hya displays classical signs of being surrounded by an accretion disk, including variable H α emission (Muzerolle et al. 2000) and excess flux over photospheric in the ultraviolet and near-infrared. In addition, it has disk signatures in the form of far-infrared (Rucinski 1985), submillimeter continuum (Weintraub, Sandell, & Duncan 1989), and CO line emission (Zuckerman, Forveille, & Kastner 1995). All of these disk indicators are large for a star as old as TW Hya, which has an age of ~ 8 Myr determined from pre-main-sequence evolutionary tracks (Webb et al. 1999). Zuckerman et al. (1995) inferred a face-on viewing geometry for the disk based on the small CO line widths they observed. Recent imaging observations do indeed reveal a circular disk. Scattered radiation from the disk has been imaged at visible and near-infrared wavelengths (Krist et al. 2000; Trilling et al. 2001), and circumstellar dust emission has been imaged at a wavelength of 7 mm using the Very Large Array (VLA; Wilner et al. 2000).

The *Hipparcos* mission measured the distance to TW Hya as 56 ± 7 pc (Wichmann et al. 1998). An eponymous association of ~ 20 star systems has been identified from

X-ray and proper-motion surveys within 10° and 10 pc of TW Hya (de la Reza et al. 1989; Webb et al. 1999; Sterzik et al. 1999; Zuckerman et al. 2001). The approximately coeval members of the TW Hya Association are among the products of recent star formation close to the Sun. Only three other members, however, have measurable far-infrared excesses from the *Infrared Astronomical Satellite (IRAS)*: HR 4796A, HD 98800, and Hen 3-600 ($L_{\text{IR}}/L_* = 0.01, 0.19,$ and 0.21 , respectively). The optical depth around TW Hya ($L_{\text{IR}}/L_* = 0.25$) is the largest and corresponds to the reprocessing expected for an optically thick disk (Adams, Lada, & Shu 1987).

The state of disks of intermediate age ($\sim 10^7$ yr) has not been well studied. The structure of the youngest disks (younger than 10^6 yr), hundreds to thousands of AU in radius around embedded protostars, has been copiously studied with millimeter interferometry (e.g., Beckwith & Sargent 1996) and visual and infrared imaging (e.g., Burrows et al. 1996; Padgett et al. 1999). There are only a few examples of older late-type stars surrounded by disks that have been spatially resolved in the near-infrared, most of which are in binary systems (e.g., Roddier et al. 1996; Koresko 1998). At ages $\gtrsim 10^7$ yr, most known disks orbit early-type stars because only in these systems do the disks scatter enough photons to be detectable (e.g., β Pic; Smith & Terrile 1984). TW Hya, thanks to its proximity to the Sun and its age, is thus an excellent laboratory for studying a disk of intermediate age around a low-mass star. This age range is thought to be critical in the evolution of the planetesimals that form the cores of gas giants and terrestrial planets (Weidenschilling & Cuzzi 1993).

2. OBSERVATIONS AND DATA ANALYSIS

2.1. NICMOS

TW Hya was observed at two different wavelength bands with the Near Infrared Camera and Multi Object Spectrometer (NICMOS) aboard the *Hubble Space Telescope*. The star was placed in the coronagraphic hole in camera 2 ($\sim 0''.076$ pixel $^{-1}$, $\sim 19''$ square field of view). The observational strategy was the same for both filters—a total of 1216 s of integration taken in three nondestructive multiple-

¹ Division of Astronomy, UCLA, Box 951562, Los Angeles, CA 90095-1562; becklin@astro.ucla.edu, ben@astro.ucla.edu.

² Department of Terrestrial Magnetism, Carnegie Institution of Washington, 5241 Broad Branch Road NW, Washington, DC 20015; weinberger@dtm.ciw.edu.

³ Steward Observatory, University of Arizona, 933 North Cherry Avenue, Tucson, AZ 85721; gschneider@as.arizona.edu, murray@as.arizona.edu, dhines@as.arizona.edu.

⁴ Department of Astronomy, University of California, Berkeley, 601 Campbell Hall, Berkeley, CA 94720; echiang@astron.berkeley.edu.

⁵ Infrared Processing and Analysis Center, MS 100-22, California Institute of Technology, Pasadena, CA 91125; lowrance@ipac.caltech.edu.

⁶ Institute for Astronomy, University of Hawaii, Honolulu, HI 96822; basmith@galileo.ifa.hawaii.edu.

readout (MULTIACCUM) sequences at each of two telescope orientations, rolled 7° with respect to each other about the target axis. To minimize time-dependent point-spread function (PSF) variations, the rolled image sets were obtained within ~ 40 minutes in a single target visibility period. The first observation was made with the F160W filter ($\lambda_{\text{central}} = 1.59 \mu\text{m}$, FWHM = $0.40 \mu\text{m}$) on 1998 August 16, and the second was made with the F110W filter ($\lambda_{\text{central}} = 1.10 \mu\text{m}$, FWHM = $0.59 \mu\text{m}$) on 1998 November 25. A summary of the observations is presented in Table 1.

Prior to each set of coronagraphic observations, two 0.86 s target acquisition frames were obtained with the F171M ($\lambda_{\text{central}} = 1.72 \mu\text{m}$, FWHM = $0.07 \mu\text{m}$) filter. Contemporaneous lamp flats and backgrounds were obtained at F160W for the purpose of locating the coronagraphic hole and enabling good flat fielding near the hole. Special coronagraphic flat fields at each band were created by modifying a standard high signal-to-noise ratio (S/N) on-orbit reference flat field. In a 16×16 pixel² region around and including the coronagraphic hole, the pixel sensitivities were measured in the F160W internal flat-field (hole finding) image, scaled to F110W if necessary, and replaced in the reference flat.

The MULTIACCUM data sets were processed with *nicred* (McLeod 1997). Dark frames prepared by the NICMOS instrument definition team were used to subtract the dark current and correct the detector shading. After bias subtraction, linearization, and flat fielding, known bad pixels were replaced with a Gaussian weighted average of neighboring pixels, and the three MULTIACCUM images from each spacecraft orientation were medianed. The best available photometric calibration was applied to the final images (F110W: $1 \text{ ADU s}^{-1} = 2.031 \times 10^{-6} \text{ Jy}$ and, referenced to Vega, $0 \text{ mag} = 1775 \text{ Jy}$; F160W: $1 \text{ ADU s}^{-1} = 2.190 \times 10^{-6} \text{ Jy}$ and $0 \text{ mag} = 1083 \text{ Jy}$). The uncertainty in this absolute photometric calibration is $\sim 2\%$ (M. Rieke 1999, private communication).

In the reduced and calibrated NICMOS images, scattered and diffracted light from the star can be much higher than the disk flux, so the instrumental PSF from an unresolved source must be subtracted. The same observing strategy, including the telescope roll, was used in our GTO program for 14 other stars at F110W and 77 at F160W. These were all processed in the same way as the TW Hya images, and we use targets that do not show extended disk emission as a library of possible PSF stars. The detailed character of the NICMOS PSF changes with time, primarily because of thermal variations in the *Hubble Space Telescope* (HST) optical assembly (Kulkarni et al. 2000) and small shifts of the camera cold mask (Krist et al. 1998); hence, some PSF star subtractions produce much lower residuals than others (Schneider et al. 2001). The software

IDP3 (Lytle et al. 1999) utilizing cubic convolution interpolation was used to register coronagraphic PSFs to both orientations of the TW Hya observations. Only stars brighter than TW Hya were considered, so the S/Ns in the PSFs were greater than that of TW Hya at every radius, and the PSF subtraction residuals were dominated by systematic uncertainties. To minimize the effect of the cold-mask shift, we considered PSFs taken within 1 month of TW Hya. Five F160W PSFs and one F110W PSF met all criteria.

The fine structure of the broadband PSF is affected by the spectral energy distribution of the source. When subtracting a reference point source, therefore, mismatches in effective temperature can result in increases in the subtraction residuals. At F160W, where several possible PSF observations existed, the chosen PSF is the K4 V star HR 8721 (= Gl 879), which is quite close to TW Hya (K7) in spectral type. At F110W, however, where many fewer PSFs were taken, the spectral type of the chosen PSF, τ^1 Eridani, is F4 V. We tested that the effect of the color mismatch is small in two ways. First, we subtracted coronagraphic PSFs of different colors and examined the residuals; two examples are plotted in Figure 1. Although color mismatch does increase the residuals, it does not introduce a false excess that could mimic a disk, nor does it significantly affect the shape of the observed TW Hya disk. Second, we created synthetic PSFs of different spectral types with Tiny Tim (Krist & Hook 1997). Since Tiny Tim models diffraction and not scattering from the coronagraph or other elements in the optical path, its PSFs isolate the effects of color alone. The Tiny Tim subtraction residuals were significant only within $0''.6$ of the star and were smaller than those from real PSF subtractions.

The dominant source of photometric uncertainty in the PSF-subtracted images results from uncertainty in how to appropriately scale the PSF to the brightness of TW Hya. There are two possible methods to determine the scaling factor: (1) the use of a priori photometry of the two stars and (2) the use of measurements made on the subtracted image, including nulling the flux in the diffraction spikes and demanding that the flux approach zero at large radii from the star. The former suffers from the fact that no images of the stars were taken in the broadband filters used for the coronagraphic imaging because the stars saturate the detector in the minimum integration time, so stellar models must be employed for the color transformations from the acquisition filters. The latter suffers from the fact that the disk contaminates the measurements.

Our PSF scalings were determined by minimizing the flux in the subtracted diffraction spikes outside the region of apparent disk flux. We scale the PSF images in ADU s^{-1} for τ^1 Eri (F110W) by 0.0099 and Gl 879 (F160W) by 0.031.

TABLE 1
LOG OF NICMOS OBSERVATIONS IN PROGRAMS 7226 AND 7233

Filter	TW Hya Visit	Date	Time (UT)	PSF Star	PSF Visit	Date
F160W.....	7/7233	1998 Aug 16	04:05–04:19	HR 8721	81/7226 ^a	1998 Aug 11
F160W.....	8/7233	1998 Aug 16	04:35–04:48	HR 8721	81/7226 ^a	1998 Aug 11
F110W.....	91/7226	1998 Nov 25	20:15–20:27	τ^1 Eri	80/7233	1998 Nov 14
F110W.....	92/7226	1998 Nov 25	20:42–20:55	τ^1 Eri	81/7233	1998 Nov 14

^a HR 8721 drifted behind the coronagraph in this visit due to the loss of lock on one guide star. We used only the first 240 s of integration in which the drift was minimal. In this time, the S/N of HR 8721 is 1.5 times that of TW Hya.

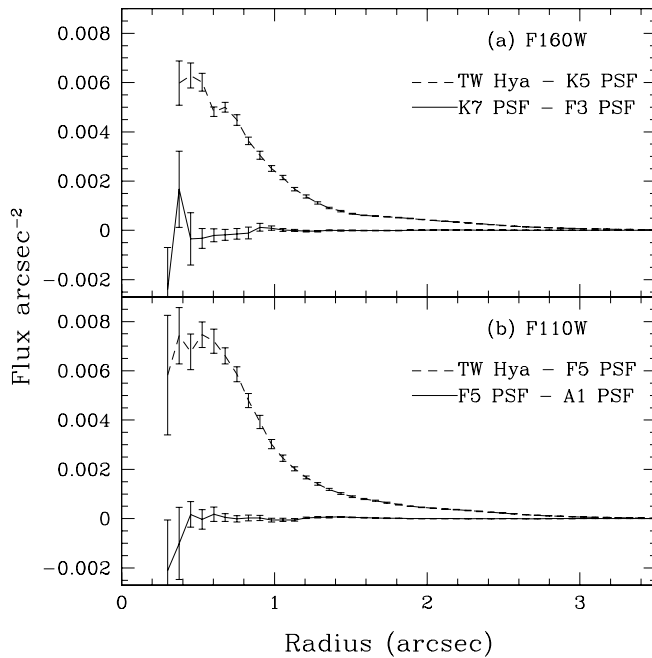


FIG. 1.—(a) Comparison of TW Hya with PSF null at F160W. The spectral types of TW Hya (K7) and its PSF (GL 879; K5) are quite close. To illustrate the effect of subtracting a PSF of a different spectral type, the null is the result of subtracting a F3-type PSF from a K7-type PSF. (b) Comparison of TW Hya and a PSF null at F110W. The spectral type of the PSF, τ^1 Eri, is F5, so color residuals should not be greater than the level demonstrated in the PSF null of part a. The PSF null in this case is of τ^1 Eri minus an A1-type PSF. For all these subtractions, comparisons with Tiny Tim show that the residuals are dominated by time-variable effects and not by color mismatch.

The uncertainty in this scaling is 3%, based on the variation between the four diffraction spikes. This uncertainty in the scaling results in approximately a 10% uncertainty in the disk photometry in each band.

2.2. Keck

Images and spectra of TW Hya were taken with the facility Long Wavelength Spectrograph (LWS; Jones & Puetter 1993) on the 10 m Keck I telescope on UT 2000 December 11 and 2001 February 4–5. During all three nights, the weather was photometric with low water-vapor optical depth. The images were limited by seeing with FWHM = $0''.57$ and $0''.50$ at $11.7 \mu\text{m}$ and $17.9 \mu\text{m}$, respectively. LWS uses a 128×128 pixel² Boeing Si:As detector and has a plate scale of $0''.08$ pixel⁻¹, resulting in a focal-plane field of view of 10.24×10.24 arcsec². It also provides a

dispersion of $0.037 \mu\text{m}$ pixel⁻¹; when combined with a 6 pixel ($0''.48$) slit, the resolution is $R \sim 120$. When viewed through the long slit, vignetting limits the field of view to $8''.5$. The infrared-bright star HR 4532 was observed immediately before or after the imaging and spectroscopy of TW Hya to provide PSF and atmospheric calibrations. Observational details are found in Table 2.

In spectroscopic mode, data were taken with the telescope secondary chopped in the same direction as the nod with a frequency of 5 Hz and amplitude of $10''$. Only the on-source chop fell on the detector. In preliminary data analysis, the images were double differenced to subtract the thermal background, and bad pixels were corrected by interpolation.

In imaging mode, data were obtained by chopping the secondary at 5 Hz and nodding after ~ 20 s. In some cases, the data were taken by chopping and nodding $5''$, so four images appear on the detector; in others the throw was $10''$, so one image appears on the detector. In either case, every double-differenced (i.e., fully background subtracted) image was centroided and recentered to remove telescope drift.

The spectra of TW Hya and of the atmospheric calibrator were extracted by fitting Gaussians in the spatial direction to the flux at every spectral pixel. The uncertainty in the flux at every wavelength was estimated from the noise in the sky on either spatial side of the long-slit image. The location of the Telluric O₃ line at $\sim 9.6 \mu\text{m}$ was measured in the sky spectra associated with both TW Hya and the standard, from which it was determined that small unrepeatabilities in the grating locator mechanism introduced a small shift in the central wavelength between the two. Before division of the TW Hya spectrum by the standard spectrum, the standard spectrum was shifted in wavelength by 2.5 pixels to match that of TW Hya. After division, the resultant spectrum was multiplied by a blackbody at the temperature of the standard star (3100 K) in order to recover the intrinsic flux distribution. The location of the telluric ozone line was measured from a cross-correlation with atmospheric data from the National Solar Observatory sunspot atlas (Wallace, Livingston, & Bernath 1994)⁷ and used for wavelength calibration.

3. RESULTS

3.1. Reflected Light

The NICMOS PSF-subtracted images of TW Hya at F110W ($1.1 \mu\text{m}$) and F160W ($1.6 \mu\text{m}$) are shown on a

⁷ Available at <ftp://argo.tuc.noao.edu/pub/atlas/spot2atl/>.

TABLE 2
LOG OF MID-INFRARED OBSERVATIONS

Mode	Object ^a	Filter Center (μm)	Filter Width (μm)	Date	Integration Time (s)	Air Mass
Imaging	TW Hya	11.7	1.0	2000 Dec 11	120	1.7
	TW Hya	11.7	1.0	2001 Feb 4	216	1.7
	PSF	11.7	1.0	2001 Feb 4	216	1.6
	TW Hya	17.9	2.0	2001 Feb 5	809	1.8
	PSF	17.9	2.0	2001 Feb 4	216	1.8
Spectroscopy	TW Hya	10.5	4.9	2000 Dec 11	408	1.7
	Atmospheric calibrator	10.5	4.9	2000 Dec 11	96	1.5

^a HR 4532 was used as the PSF and atmospheric calibrator. The bright star HR 3748 ($11.7 \mu\text{m}$ flux density = 53.6 Jy) was observed for photometric calibration.

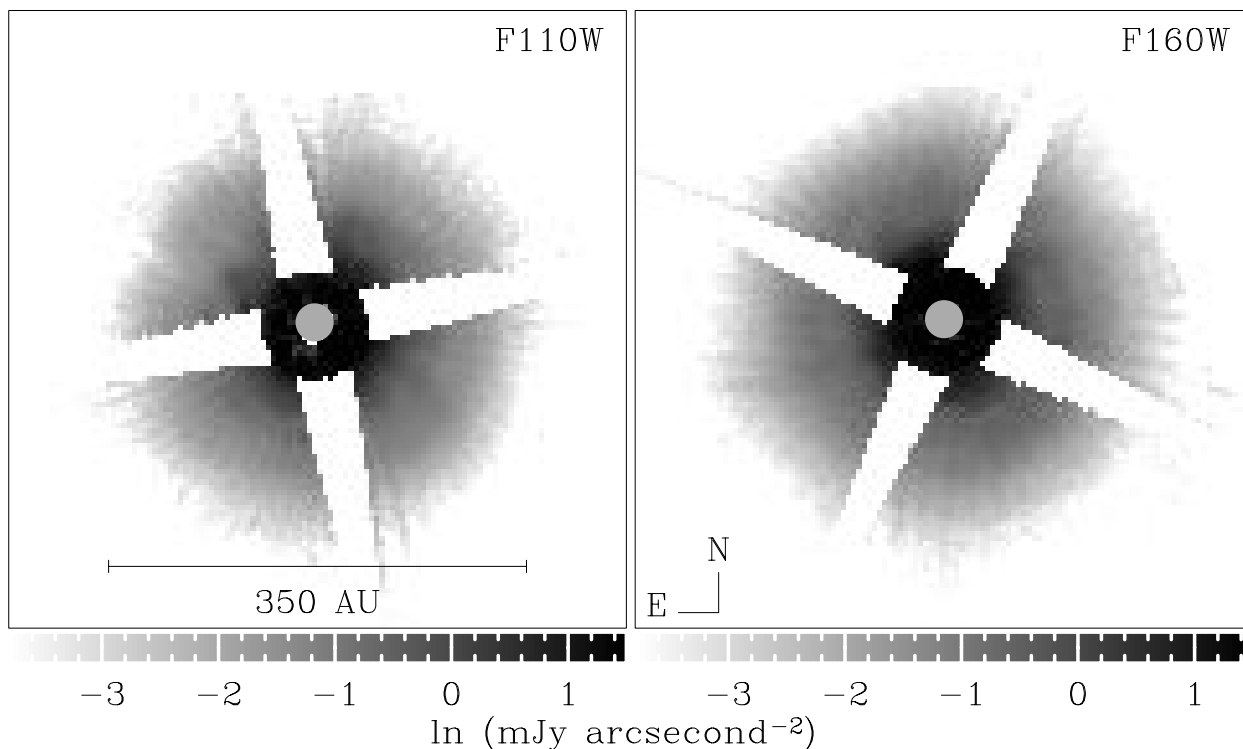


FIG. 2.—*Left*: PSF-subtracted, roll-combined image of TW Hya at F110W; *Right*: PSF-subtracted, roll-combined image of TW Hya at F160W, both shown with a natural logarithmic stretch and on the same spatial scale and orientation. This stretch is employed since the disk falls off as a power law and so it highlights the outer disk. The size (radius $0\prime.3$) and location of the coronagraph are shown with the central gray circle. The diffraction spikes have been masked in regions where their noise is greater than the disk signal. They have a tapered shape because pixels obscured at one telescope orientation were replaced with those not obscured at the other orientation.

natural logarithmic stretch in Figure 2. The disk becomes visible just outside the coronagraph and continues out to a radius of $4''$ (~ 230 AU). The noise computed in the background of the images is 21.1 and 21.2 mag arcsec $^{-2}$ at F160W and F110W, respectively. In the disk, the noise is dominated by subtraction residuals. The spatial resolution of these images is $0\prime.15$ at F160W and $0\prime.12$ at F110W.

The diffraction spikes from the stellar cores are particularly sensitive to time-dependent instrument and telescope variations and never subtract out perfectly. Where possible, the pixels corrupted by the spikes in images from one telescope orientation were replaced by uncorrupted pixels from the other orientation. This results in the tapered appearance of the spikes in the final images. The spikes were not masked in the central $0\prime.9$ because, even though they are quite noisy, the very bright inner disk of TW Hya can still be significantly detected above them in the region from $0\prime.38$ (just outside the edge of the coronagraphic hole) to $0\prime.9$.

The total disk flux densities were measured in an annulus between radii of $0\prime.38$ and $4''$ (22–228 AU) to be 17.4 ± 1.8 mJy (12.5 ± 0.1 mag) at F110W and 21.6 ± 2.2 mJy (11.7 ± 0.1 mag) at F160W. At both wavelengths, the pixels masked by the diffraction spikes were replaced by the average value of the flux density at their radii and included in the photometry reported above. The quoted uncertainties are not dominated by photon-counting statistics but rather by the systematic uncertainty in how to scale the PSF stars to TW Hya. The measured ratios of scattered to stellar light are 0.024 and 0.021 at F110W and F160W, respectively. The surface brightness peaks at a radius of $0\prime.5$ (29 AU) at 4.5 ± 1.2 mJy arcsec $^{-2}$ at F110W and 5.7 ± 1.4 mJy arcsec $^{-2}$ at F160W and declines smoothly with radius.

To measure any ellipticity in the disk, the radii of seven independent isophotal contours were calculated as a function of azimuthal angle in the F160W image. For a more significant result, the contours were normalized to a radius of 1 and averaged in 16 azimuthal bins. The average isophote was fit with an ellipse using eccentricity (i.e., inclination) and position angle as two free parameters. The resulting best fit had $e = 0.025 \pm 0.014$. If this ellipticity is interpreted as the result of the inclination of an intrinsically circular disk, the measured inclination is of marginal significance, but a robust 3σ upper limit to the inclination is 4° from face-on.

The azimuthally averaged disk surface brightnesses at both wavelengths are shown in Figure 3. Between radii of 40 and 150 AU, the disk at both wavelengths is well fit by a single power law, $r^{-2.6 \pm 0.1}$ (the solid lines in Fig. 3). Also seen at F160W, however, is a “wobble” in the surface brightness centered at $1\prime.5$ (85 AU). Beyond 150 AU, the disk falls off more sharply. Within 40 AU, it appears to flatten.

To obtain the color of the disk, the images at F110W and F160W were ratioed. Since the images in the two filters were taken at quite different telescope orientations, the diffraction spikes corrupt 50% of the ratioed image. There are no significant gradients in the color as a function of radius. The F110W–F160W color averaged over the pixels free from diffraction spike contamination is 0.77 ± 0.10 mag.

Since TW Hya was never observed with the NICMOS F110W and F160W filters without the coronagraph, the color of the star at these two NICMOS bands was estimated based on a stellar photosphere model by Kurucz (1993). The F171M magnitude of the star was measured from the acquisition images to be 7.39 ± 0.04 mag from

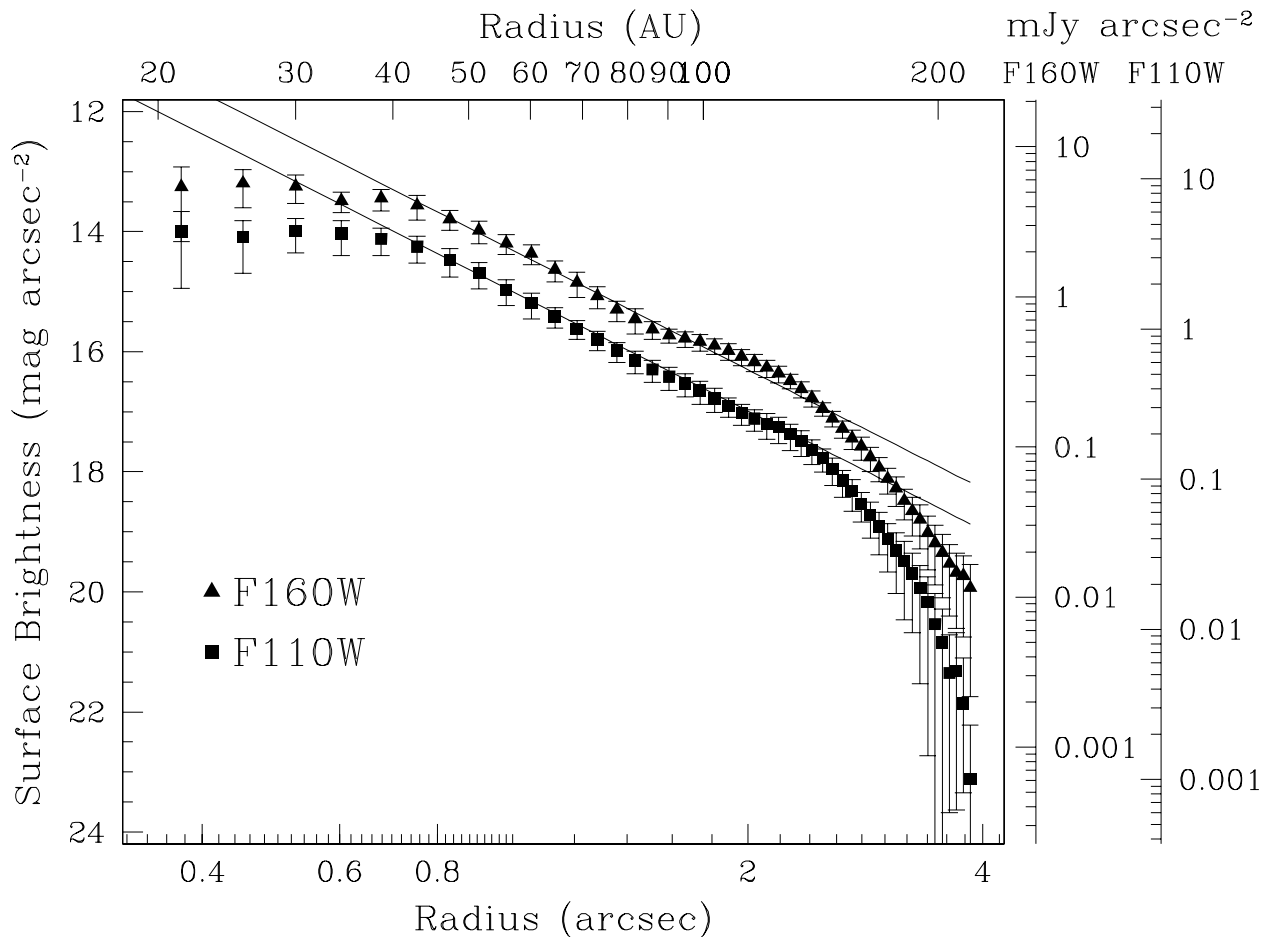


FIG. 3.—Surface brightness of TW Hya at both 1.1 and 1.6 μm as a function of radius. The black lines show a power law of $r^{-2.6}$ fitted between 40 and 150 AU and extrapolated to other radii. The error bars on each point represent the standard deviation of all the pixels at the given radius in an annulus 1 pixel wide.

both the 1998 August and November data. The *UBVRI* variability of TW Hya, which amounts to ~ 0.5 mag at *V* and decreases toward the red, has been examined in detail and shown to have an overall period of 1–2 days with much shorter episodes of rapid change (Rucinski & Krautter 1983; Mekkadon 1998; Herbst & Koret 1988). The star becomes bluer by up to 20% as it brightens. The near-infrared variability has not been thoroughly studied, but its level is expected to be low if the underlying cause of the variation is from hot spots. The high level of consistency in the photometry of our acquisition images from the two dates implies that the star did not vary at 1.7 μm between August and November. We assume the star was similarly stable at 1.1 and 1.6 μm .

A Kurucz stellar atmosphere model with $T_{\text{eff}} = 3925$ K, $\log(g) = 4$, and $\log(Z) = 0$ was used to extrapolate the F171M magnitude to F110W and F160W, giving 8.47 and 7.55 mag, respectively. The same model gives $H = 7.53$ and $J = 8.35$ mag (in the CIT system), which are 10% brighter than the values given by Rucinski & Krautter (1983), which had an uncertainty of 5%–10%. The inferred $J-H$ color, 0.82, is identical to that obtained by Rucinski & Krautter (1983), so we believe the model extrapolation to the NICMOS filters to be accurate. The F110W–F160W stellar color is thus 0.92 mag, while the color of the disk is 0.77 ± 0.10 mag, so the disk color appears to be marginally (1.3 σ) blue.

Using *HST*/Wide Field Planetary Camera 2 (WFPC2), Krist et al. (2000) also found a slightly blue color for the disk at visual wavelengths (0.6 and 0.8 μm) in images made when the star was as bright as it has ever been recorded. The best estimate of color should come from the largest wavelength range, i.e., 0.6–1.6 μm . Over the disk region between 0".5 and 3", $F606W - F160W = 2.6 \pm 0.2$. For TW Hya, $F606W - F160W = 2.5$, so the disk appears to scatter neutrally over this 1 μm wavelength baseline.

3.2. Thermal Emission

The radial profiles of TW Hya in thermal emission at 11.7 and 17.9 μm are shown in Figure 4 compared with images of the PSF star. TW Hya appears to be the same size as the PSF, i.e., unresolved, at both wavelengths. Integrated flux densities were measured in a synthetic aperture of radius 2".4 and were 0.72 ± 0.04 Jy at 11.7 μm and 1.45 ± 0.08 Jy at 17.9 μm . The measurement uncertainties reflect both statistical and photometric calibration contributions. These flux densities agree very well with those given in the *IRAS* Faint Source Catalog (Moshir et al. 1990) at 12 and 25 μm interpolated to our wavelengths of observation. Thus, all of the mid-infrared flux in the *IRAS* beam arises from quite close to the star. Using a Kurucz model of a K7 photosphere (see Fig. 5) to predict the *L*-band flux and then assuming Rayleigh-Jeans falloff from 3.5 to 18 μm , we determine the stellar flux density at 11.7 and 17.9 μm as 31

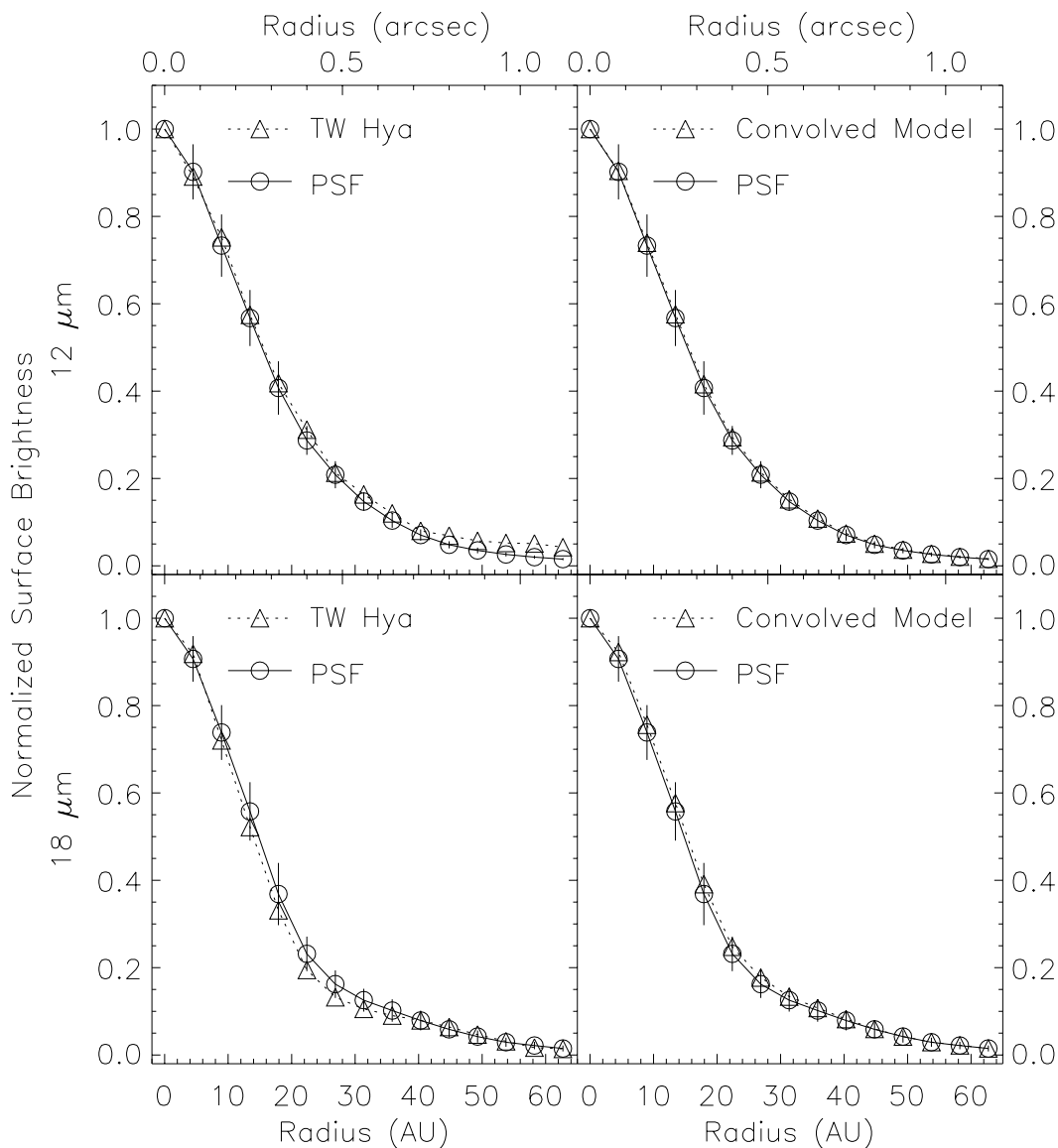


FIG. 4.—In the left panels, the azimuthal profiles of our Keck point-spread function star 11.7 (*top row*) and 17.9 μm (*bottom row*) are compared to profiles of our images of TW Hya. In the right panels, the model described in § 4.2.1 convolved with our PSF is compared to the PSF. At each radius, the error bars show the standard deviation about the mean value of pixels in a 1 pixel wide annulus. The PSF is evidently oversampled at these wavelengths, and the first Airy minimum can just be seen in the 17.9 μm profile at $0''.48$. TW Hya is unresolved (*left*). This result is consistent with the model (*right*).

and 13 mJy, respectively. The mid-infrared color temperature of the disk is 214 K from our measurements.

The 8 – 13 μm spectrum of TW Hya is shown in Figure 6. The 11.7 μm flux density above was used to normalize the spectrum, since the full width of that filter is contained in the spectral range. There is a broad hump in this region that, similarly to Sitko, Lynch, & Russell (2000), we attribute to emission by a combination of amorphous and crystalline silicates.

3.3. Detection Limits for Companions

Multiplicity in the TW Hya association as a whole is $\geq 50\%$, including stellar and substellar objects (Zuckerman et al. 2001), although TW Hya itself has no known companion. At the young age of TW Hya any substellar companions would be quite bright in the infrared, so our NICMOS images provide a sensitive way to search for such objects.

We subtracted the two orientations of our F160W data. While the stellar PSF, the instrumental scattering function, and detector artifacts rotate with the aperture, any real features in the unocculted area of the detector are unaffected by a change in the telescope/camera orientation. Subtraction of these two images has been shown to significantly reduce residual PSF background light (Schneider et al. 1998). Furthermore, since the TW Hya disk is almost face-on, it nulls out nearly perfectly in the roll subtraction, leaving higher noise but no excess flux. In our data, the roll was only 7° , so point sources in the roll subtraction are separated by more than their FWHM for radii greater than $1/2$ (67 AU). For smaller radii, the roll subtraction was not useful for point-source detection and we used the PSF-subtracted images discussed already. In both regions, we assessed the observability of point sources by planting Tiny Tim PSFs and measuring the magnitude that could be

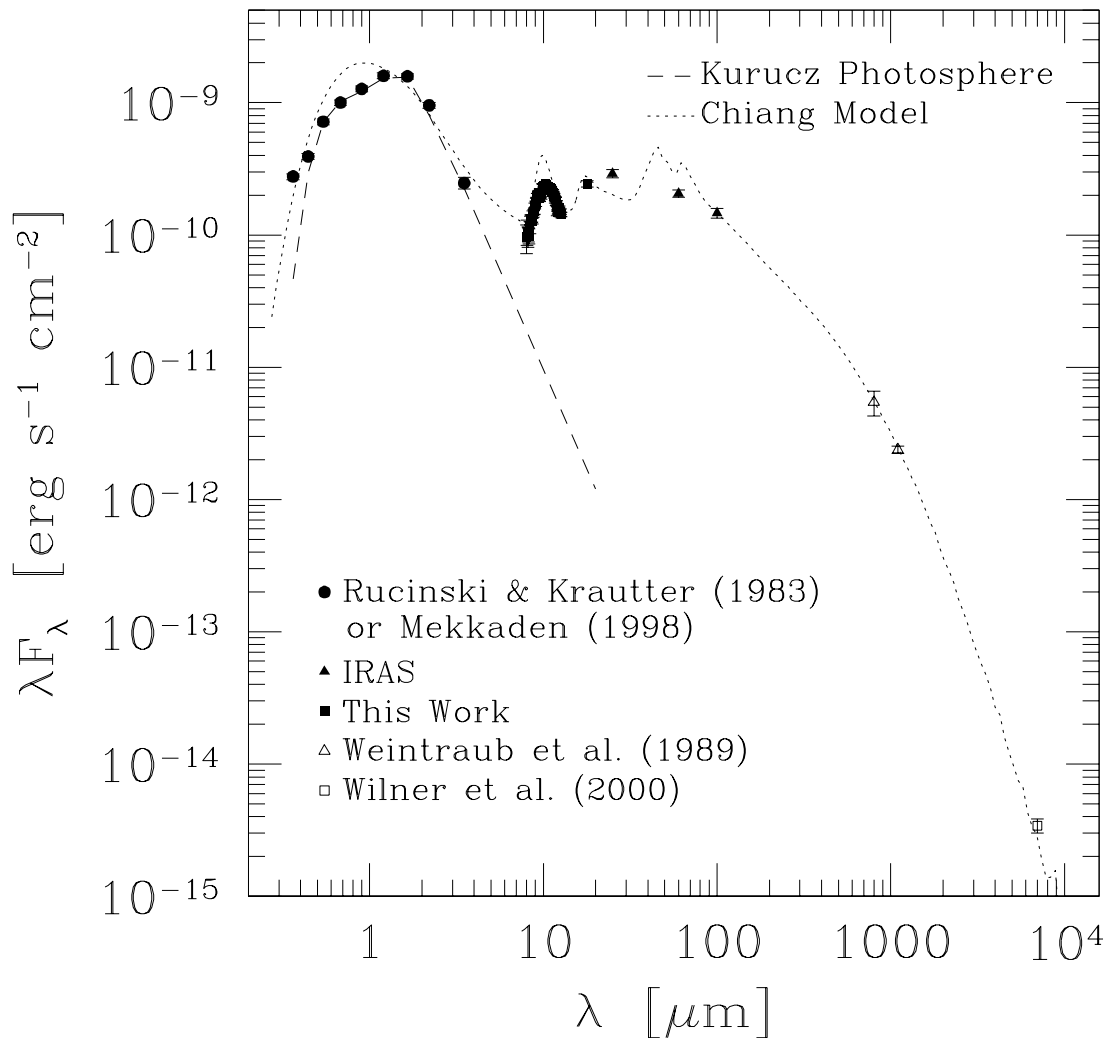


FIG. 5.—Measured spectral energy distribution for TW Hya compared to that of a Kurucz model stellar photosphere with $T_{\text{eff}} = 3925$ K, $\log g = 4.0$, and solar metallicity (*dashed line*) and the § 4.2.1 disk model (*dotted line*). There is no thermal excess at wavelengths $\leq 3 \mu\text{m}$, so dust does not extend to within 0.05 AU.

recovered at more than 3σ significance. No point sources were found within $3/4$ of TW Hya. The F160W detection limits are shown in Figure 7.

4. DISCUSSION

4.1. Disk Morphology

Given the large fraction (0.25) of the stellar luminosity reradiated in the mid- and far-infrared, the disk must be optically thick. For single scattering by a geometrically flat and optically thick disk, the flux density per square arcsecond would be proportional to r^{-3} (Whitney & Hartmann 1992). This is somewhat steeper than the $r^{-2.6}$ we fit in the 40–150 AU annular region and suggests that the disk is instead flared. Perhaps the strongest argument in favor of disk flaring is that the reflected-light surface brightness throughout this annulus is much larger than predicted by a flat-disk model.

A warm optically thick disk composed of well-mixed dust and gas will naturally flare as a consequence of vertical hydrostatic equilibrium (Kenyon & Hartmann 1987). If dust and gas are well mixed and in interstellar proportions, then the height at which stellar photons are scattered is roughly proportional to the vertical pressure scale height.

In this case, the scattering height scales as r^γ , where $\gamma \approx 1.2$ – 1.4 (Chiang & Goldreich 1997; D’Alessio et al. 1998; Chiang et al. 2001). Such a well-mixed, flared disk has a scattering brightness profile that scales approximately as r^{-2} (Whitney & Hartmann 1992), significantly shallower than the average TW Hya profile at disk radii greater than 40 AU. The discrepancy could reflect vertical settling of dust with respect to the gas, such that the actual scattering height at these radii is characterized by $\gamma < 1$.

The F160W surface brightness profile between 80 and 130 AU scales like r^{-2} . This annulus corresponds to the “zone 3” defined by Krist et al. (2000) (Fig. 8), where the visual scattered light also flattens out in their images. The appearance of the same feature in data from two different instruments lends credibility to the idea that this feature is real. Such a variation in the slope of the surface brightness profile might reflect an undulation or ripple in the height of the disk surface; at $40 \text{ AU} \lesssim r \lesssim 80 \text{ AU}$, the disk surface might be concave down, while at $80 \text{ AU} \lesssim r \lesssim 130 \text{ AU}$, the disk might be concave up. Distortions of the disk may be caused by instabilities afflicting passively heated disks (Chiang 2000; Dullemond 2000) or by dynamical effects created by a massive body orbiting in the disk. The detection limit on a massive body at 100 AU from the star is

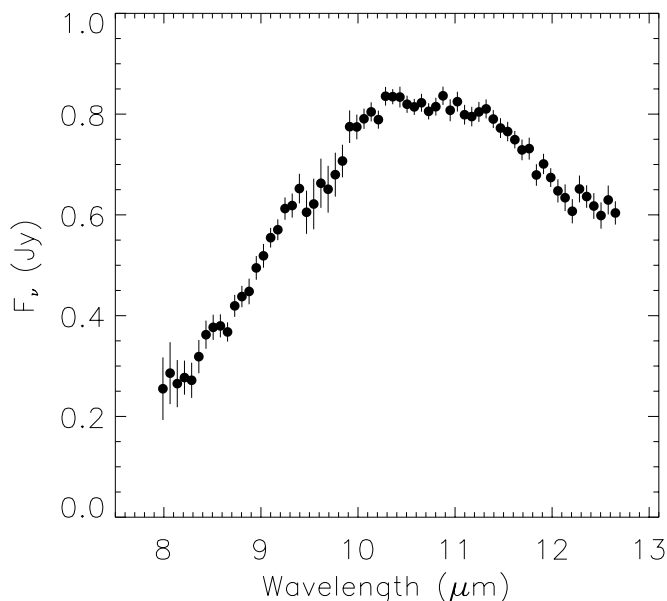


FIG. 6.—The 8–12.5 μm spectrum of TW Hya with resolution $\lambda/\Delta\lambda \sim 120$. The emission in this region shows the character of amorphous silicates (peaking at $\sim 9.6 \mu\text{m}$) mixed with crystalline silicates (with peaks at $\sim 11.2 \mu\text{m}$). Around 9.7 μm , the small depression in flux is not real but is caused by imperfect calibration of the time variable atmospheric Ozone emission. The overall normalization is set to make the 11.7 μm flux equal to that measured in the imaging. The overall shape agrees well with that observed by Sitko et al. (2000), but the evidence for crystalline components is even more compelling in the flatness of the spectrum longward of 10 μm .

$3 M_J$. Beyond 150 AU, the surface brightness profile is significantly steeper than r^{-3} . The outer disk is probably completely shadowed.

The face-on geometry of the disk and the average NICMOS data power law for the disk surface brightness are consistent with the WFPC2 data of Krist et al. (2000). Their average power law in the same 40–150 AU region (see Fig. 8) is -2.4 at F606W (0.6 μm) and -2.6 at F814W (0.8

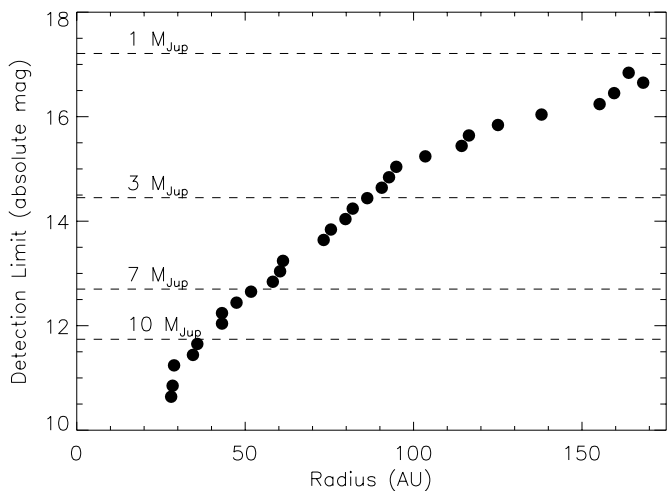


FIG. 7.—Limiting F160W absolute magnitude of a detectable point source as a function of distance from TW Hya. The masses as a function of absolute magnitude are based on an age of 10 Myr and cooling models of Burrows et al. (1997) and are accurate to ~ 0.3 mag (A. Burrows 2000, personal communication). At the radius of ~ 85 AU where the dip in disk surface brightness occurs, the limit is $\sim 3 M_J$. No point source was detected within $4''$ of TW Hya.

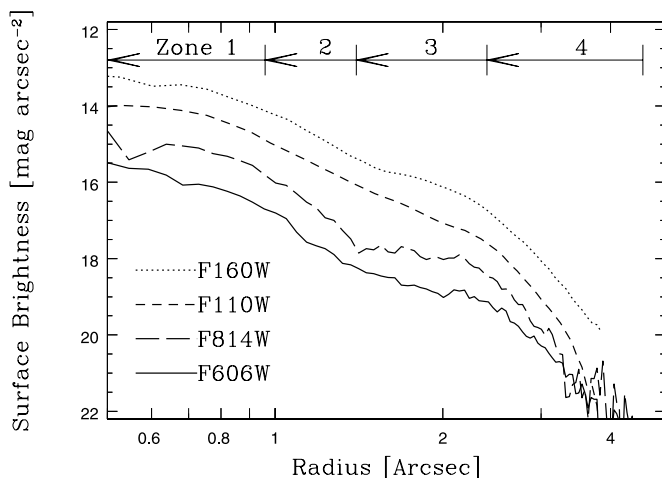


FIG. 8.—Profile of TW Hya disk observed with NICMOS compared to that observed with WFPC2 by Krist et al. (2000). Both sets of observations show a small depression in surface brightness at $1''.5$ as well as the same overall slope of the surface brightness.

μm). In addition, the geometry of the disk seen in both *HST* data sets is consistent with the general morphology reported by Trilling et al. (2001) from ground-based observations. There are notable differences, however, between the NICMOS and Trilling et al. data. At their innermost detectable radius of $0''.94$, they report a peak surface brightness at *H* band of 6.8 ± 1.1 mJy arcsec $^{-2}$. At this same radius, which is well outside our coronagraph, and using the F160W filter, which is very similar to *H* band, we measure 2.5 ± 0.4 mJy arcsec $^{-2}$. In addition, they measured a total disk flux density in the $0''.94$ – $4''$ region of 21.6 ± 3.5 mJy, whereas we measure 12.0 ± 1.2 mJy in that same region. The Trilling et al. surface brightness power-law index, -3.3 ± 0.3 , is discrepant by 2.5σ with the NICMOS index of -2.6 ± 0.1 . Systematic uncertainties in their ground-based PSF subtraction under conditions of $0''.8$ seeing may be responsible for the discrepancies.

The large optical depth of the disk makes it difficult to use the scattered light to estimate the density of grains. At any given position in the disk, visible and near-infrared stellar radiation penetrates to an optical depth of 1. In contrast, the disk is presumably optically thin at millimeter wavelengths, so millimeter images of the dust emission trace the true surface density.

4.2. Composition

To elucidate the dust composition, we combine information from the spectral energy distribution, mid-infrared imaging, and mid-infrared spectroscopy.

4.2.1. SED Fitting Compared to Mid-Infrared Imaging

A simple model of the disk using grains that absorb and emit like blackbodies in thermal equilibrium with a star of luminosity $0.3 L_{\odot}$ predicts a temperature of 214 K, the 11.7–17.9 μm color temperature, at a distance of only 0.9 AU ($0''.04$). If the entire disk could be described by such grains, it would therefore not be surprising that it appears pointlike. In more sophisticated models of passive circumstellar disks, Chiang & Goldreich (1997) and Chiang et al. (2001) predict the mid-infrared flux emitted by a disk as a function of radius. In their two-layer disk models, the hotter

disk surface layer is heated by direct exposure to starlight, while the cooler disk interior is heated by radiation from the surface. To compare predictions of their models with our mid-infrared images, we modeled TW Hya after the prescription of Chiang et al. (2001), which accounts explicitly for grain size distributions and laboratory-based silicate and water ice opacities. Our procedure was to first select disk parameters so as to reproduce the observed SED only. In fitting the disk parameters, no regard is given to any imaging data. Only after a disk model is chosen that provides a satisfactory fit to the SED do we derive surface brightness profiles at 11.7 and 17.9 μm based on our fitted model disk. These profiles are convolved with our respective PSFs and compared to our images of TW Hya.

Figure 5 displays the observed and fitted SEDs of TW Hya. Model input parameters are given in Table 3. For additional details of the model, see Chiang et al. (2001). The SED model predicts that 99.8% of the 12 μm flux density and 94.6% of the 18 μm flux density arise within a radius of 9 AU (2 pixels) of the star. As is shown in Figure 4, at the resolution of the Keck Telescope, no extended emission is predicted by the model. This is consistent with the observations in which no extension is observed.

Outside 0.2 (2) AU, silicate cores are mantled by water ice in the disk interior (surface). The remarkably large grains in the disk interior, consisting of millimeter–centimeter sized cores, and the large total condensable mass in the disk of $0.0014 M_{\odot} = 470 M_{\oplus}$ were necessary to fit the millimeter-wave SED measured by Weintraub et al. (1989) and Wilner et al. (2000). The measurement at the particularly long wavelength of 7 mm constrains the grain size distribution in the disk interior to be significantly flatter than the standard interstellar law of $dN/da \propto a^{-3.5}$ and to possess an upper size cutoff of 6 mm. Had we employed a grain-size distribution that was much steeper than a^{-1} and that had an upper size cutoff smaller than $a = 6$ mm, the model fluxes between 1.3 and 7 mm would have been too low compared to the measurements. Our fitted grain-size distributions in the disk interior are subject to the well-known degeneracy between grain size and disk surface density (see, e.g., Chiang et al. 2001); reducing the grain sizes or steepening the size distribution increases the fitted dust surface mass density. Increasing the fitted dust surface density, however, would threaten to make the disk gravitationally unstable if gas and dust are present in interstellar proportions in TW Hya. We draw the model-dependent conclusion that grain growth has indeed occurred in the TW Hya disk.

For the particular grain mixture of millimeter- to centimeter-sized olivine spheres mantled with water ice employed by our model, $\kappa_{1.1 \text{ mm, dust}} = 0.84 \text{ cm}^2 \text{ g}^{-1}$ and $\kappa_{7 \text{ mm, dust}} = 0.14 \text{ cm}^2 \text{ g}^{-1}$. A somewhat lower dust mass of

$\sim 130 M_{\oplus}$ was derived by Wilner et al. (2000) and Trilling et al. (2001) using the same observational data. The difference arises largely because their assumed dust opacities were ~ 3 times greater than ours (we have multiplied their opacities by 100 to isolate the dust component). Their values were based on the Hildebrand (1983) measurement of $\kappa_{250 \mu\text{m, dust}} = 10 \text{ cm}^2 \text{ g}^{-1}$ in the dark molecular cloud NGC 7023 and extrapolated to longer wavelengths with $\kappa_{\nu, \text{dust}} \propto \nu^{\beta}$, where β is taken to be 1.0 by Wilner et al. and 0.9 by Trilling et al. The assumed similarity between dust in NGC 7023 and dust in TW Hya has no direct observational evidence.

Pollack et al. (1994) showed that a single power-law description of the opacity is inaccurate for real dust materials. They computed opacities for a variety of grain species, including water ice, silicates, organics, iron, and troilite. For their “Composite (50%)” grains, extrapolated values of $\kappa_{7 \text{ mm, dust}}$ range between 0.03 and 0.06 $\text{cm}^2 \text{ g}^{-1}$, assuming that the values of β that they compute between 650 μm and 2.3 mm can be extended to 7 mm. These opacities are a factor of ~ 3 smaller than the ones employed in our disk model fit and a factor of 5–10 smaller than the ones adopted by Wilner et al. (2000) and Trilling et al. (2001).

Krist et al. (2000) model only $\sim 33 M_{\oplus}$ of ISM-like dust to reproduce their observed surface brightness profiles in scattered light at $\lambda = 0.6$ and 0.8 μm . The profiles depend more strongly on the distribution of dust at high altitude above the midplane than on the distribution of dust in the midplane where most of the mass probably resides. Krist et al. assume a Gaussian vertical density profile for micron-sized dust. Substantially more dust, however, could reside at the midplane of their disk model without detracting from the goodness of their surface brightness fits. Thus, their $\sim 33 M_{\oplus}$ could easily represent a lower limit on the actual dust mass.

We conclude that the TW Hya disk probably contains several hundred Earth masses of condensed silicates and ices. This dust mass is several times larger than the typical dust masses estimated for T Tauri star disks in the Taurus and Ophiuchus star-forming regions on the basis of 1.3 mm dust continuum observations (Osterloh & Beckwith 1995; Andre & Montmerle 1994). Large centimeter-sized grains were necessary to fit the $\sim \nu^{3.5}$ slope of the millimeter-wave SED. A grain-size distribution with smaller grains is characterized by a significantly steeper slope, $\sim \nu^{4-5}$, and is difficult to reconcile with the observations. The presence of these very large particles is good evidence for grain growth within the disk.

Total mass estimates for TW Hya’s disk in the literature vary by another 2 orders of magnitude depending on the assumed gas:dust ratio. The standard interstellar gas:dust mass ratio of 100:1 may be incorrect for an older disk like that around TW Hya. Kastner et al. (1997) find only $11 M_{\oplus}$ in H_2 gas based on ^{13}CO observations and a standard interstellar H_2/CO ratio. The low mass-accretion rate estimated by Muzerolle et al. (2000), an order of magnitude less than for typical T Tauri stars, also suggests that the gas in this system has been depleted. The gas-to-dust mass ratio does not formally enter into our model SED-fitted disk; only enough gas and/or vertical circulation of gas is assumed to lift dust grains ~ 3 –5 vertical scale heights above the midplane to comprise the flared, superheated disk atmosphere. If we assume the primordial TW Hya disk had the canonical 100:1 gas to dust ratio, then it once contained

TABLE 3
PARAMETERS OF TW HYA DISK MODEL

Parameter	Value
Maximum grain radius in surface (μm)	1
Maximum grain radius in interior (μm)	6000
Grain core size distribution (dN/da):	
In disk interior	$\propto a^{-1}$
In disk surface	$\propto a^{-3.5}$
Dust surface mass density [$(a/\text{AU})^{-1} \text{ g cm}^{-2}$]	10
Inner disk radius (AU)	0.05
Outer disk radius (AU)	200

0.14 M_{\odot} . This early disk with $\sim 25\%$ of the star's mass would have been marginally gravitationally stable.

4.2.2. Mid-Infrared Spectrum

The broad silicate emission feature cannot be explained by amorphous silicates alone since they have a pronounced peak at $9.6 \mu\text{m}$ and fall off rapidly to longer wavelengths. Our spectrum agrees very well with the published result of Sitko et al. (2000), who note the near absence of a peak at $11.2 \mu\text{m}$, within the uncertainties of their data. Our spectrum hints at a peak at $11.2 \mu\text{m}$; furthermore, to create the full width of the feature requires substantial flux longward of $10 \mu\text{m}$. Crystalline species are probably responsible. Data of this spectral resolution are inadequate to constrain the exact crystalline structure, however. Magnesium and iron-rich species all have peaks in the $10\text{--}11.3 \mu\text{m}$ region (Jäger et al. 1998). Silicate emission features become less prominent as the grains get larger, so that by a size of $\sim 5 \mu\text{m}$ their mid-infrared spectrum is nearly flat (Skinner, Barlow, & Justtanont 1992). The TW Hya spectrum suggests that its emitting grains must therefore be $\lesssim 5 \mu\text{m}$ in size.

5. CONCLUSIONS

TW Hya is surrounded by an optically thick dust disk that must be flared to account for the large apparent size of the disk seen in scattered light and for its thermal SED. A ripple in the surface brightness at 85 AU and the steep decline in surface brightness beyond 150 AU could be the result of thermal instabilities or dynamical effects. However, no companion to TW Hya is detected down to a mass of $\sim 10 M_J$ at distances greater than 50 AU from the star.

Although TW Hya looks like a classical T Tauri star in terms of its H α emission, its disk shows signs of evolution. To fit the large submillimeter and millimeter flux densities measured from TW Hya, our SED models require a grain size distribution in the disk interior dominated by large millimeter- and centimeter-sized icy grains. Large grains, which dominate the mass of the disk, presumably grew from coagulation of smaller grains in the disk. The initial mass of TW Hya's disk in gas and dust may be several times the typical T Tauri star disk mass, which may help account for its long, ~ 8 Myr, lifetime. The thermal emission remains spatially unresolved at the resolution of the Keck Telescope, in accord with theoretical expectations.

We thank John Krist and Mike Sitko for providing their data in digital form, our anonymous referee for insightful comments on the manuscript, and the Keck staff for help with LWS. This work was supported by NASA grant NAG 5-3042 to the NICMOS IDT and by a Hubble Fellowship grant to E. I. C. This paper is based on observations with the NASA/ESA *Hubble Space Telescope*, obtained at the Space Telescope Science Institute, which is operated by the Association of Universities for Research in Astronomy, Inc., under NASA contract NAS 5-26555. This paper is also based on observations at the W. M. Keck Observatory, which is operated as a scientific partnership between the California Institute of Technology, the University of California, and the National Aeronautics and Space Administration, and was made possible by the generous financial support of the W. M. Keck Foundation.

REFERENCES

- Adams, F. C., Lada, C. J., & Shu, F. H. 1987, *ApJ*, 312, 788
 Andre, P., & Montmerle, T. 1994, *ApJ*, 420, 837
 Beckwith, S. V. W., & Sargent, A. I. 1996, *Nature*, 383, 139
 Burrows, A., et al. 1997, *ApJ*, 491, 856
 Burrows, C. J., et al. 1996, *ApJ*, 473, 437
 Chiang, E. I. 2000, Ph.D. thesis, Caltech
 Chiang, E. I., & Goldreich, P. 1997, *ApJ*, 490, 368
 Chiang, E. I., Joungh, M. K., Creech-Eakman, M. J., Qi, C., Kessler, J. E., Blake, G. A., & van Dishoeck, E. F. 2001, *ApJ*, 547, 1077
 D'Alessio, P., Canto, J., Calvet, N., & Lizano, S. 1998, *ApJ*, 500, 411
 de la Reza, R., Torres, C. A. O., Quast, G., Castilho, B. V., & Vieira, G. L. 1989, *ApJ*, 343, L61
 Dullemond, C. P. 2000, *A&A*, 361, L17
 Henize, K. G. 1976, *ApJS*, 30, 491
 Herbst, W., & Koret, D. L. 1988, *AJ*, 96, 1949
 Hildebrand, R. H. 1983, *QJRAS*, 24, 267
 Jäger, C., Molster, F. J., Dorschner, J., Henning, T., Mutschke, H., & Waters, L. B. F. M. 1998, *A&A*, 339, 904
 Jones, B., & Puetter, R. 1993, *Proc. SPIE* 1946, 610
 Kastner, J. H., Zuckerman, B., Weintraub, D. A., & Forveille, T. 1997, *Science*, 277, 67
 Kenyon, S. J., & Hartmann, L. 1987, *ApJ*, 323, 714
 Koresko, C. D. 1998, *ApJ*, 507, L145
 Krist, J. E., & Hook, R. N. 1997, in *Proc. 1997 HST Calibration Workshop: With a New Generation of Instruments*, ed. S. Casertano et al. (Baltimore: STScI), 192
 Krist, J. E., Golimowski, D. A., Schroeder, G., & Henry, T. J. 1998, *PASP*, 110, 1046
 Krist, J. E., Stapelfeldt, K. R., Ménard, F., Padgett, D. L., & Burrows, C. J. 2000, *ApJ*, 538, 793
 Kulkarni, V. P., Hill, J. M., Schneider, G., Weymann, R. J., Storrie-Lombardi, L. J., Rieke, M. J., Thompson, R. I., & Januzzi, B. 2000, *ApJ*, 536, 36
 Kurucz, R. 1993, CD-ROM 13, GSFC (Cambridge: SAO)
 Lytle, D., Stobie, E., Ferro, A., & Barg, I. 1999, in *ASP Conf. Ser. 172, Astronomical Data Analysis Software and Systems 8*, ed. D. M. Mehringer, R. L. Plante, & R. A. Roberts (San Francisco: ASP), 445
 MacLeod, B., A. 1997, in *Proc. 1997 HST Calibration Workshop: With a New Generation of Instruments*, ed. S. Casertano et al. (Baltimore: STScI), 281
 Mekkaden, M. V. 1998, *A&A*, 340, 135
 Moshir, M., et al. 1990, *IRAS Faint Source Catalog, Ver. 2.0* (Greenbelt: NASA/GSFC)
 Muzerolle, J., Calvet, N., Briceño, C., Hartmann, L., & Hillenbrand, L. 2000, *ApJ*, 535, L47
 Osterloh, M., & Beckwith, S. V. W. 1995, *ApJ*, 439, 288
 Padgett, D. L., Brandner, W., Stapelfeldt, K. R., Strom, S. E., Terebey, S., & Koerner, D. 1999, *AJ*, 117, 1490
 Pollack, J. B., Hollenbach, D., Beckwith, S., Simonelli, D. P., Roush, T., & Fong, W. 1994, *ApJ*, 421, 615
 Roddier, C., Roddier, F., Northcott, M. J., Graves, J. E., & Jim, K. 1996, *ApJ*, 463, 326
 Rucinski, S. M. 1985, *AJ*, 90, 2321
 Rucinski, S. M., & Krautter, J. 1983, *A&A*, 121, 217
 Schneider, G., Becklin, E. E., Smith, B. A., Weinberger, A. J., Silverstone, M., & Hines, D. C. 2001, *AJ*, 121, 525
 Schneider, G., Thompson, R. I., Smith, B. A., & Terrile, R. J. 1998, *Proc. SPIE*, 3356, 222
 Sitko, M. L., Lynch, D. K., & Russell, R. W. 2000, *AJ*, 120, 2609
 Skinner, C. J., Barlow, M. J., & Justtanont, K. 1992, *MNRAS*, 255, 31P
 Smith, B. A., & Terrile, R. J. 1984, *Science*, 226, 1421
 Sterzik, M. F., Alcalá, J. M., Covino, E., & Petr, M. G. 1999, *A&A*, 346, L41
 Trilling, D. E., Koerner, D. W., Barnes, J. W., Ftaclas, C., & Brown, R. H. 2001, *ApJ*, 552, L151
 Wallace, L., Livingston W., & Bernath, P. 1994, *An Atlas of the Sunspot Spectrum from 470 to 1233 cm⁻¹ (8.1 to 21 microns) and the Photospheric Spectrum from 460 to 630 cm⁻¹ (16 to 22 microns)*, NSO Tech. Rep. 1994-01
 Webb, R. A., Zuckerman, B., Platais, I., Patience, J., White, R. J., Schwartz, M. J., & McCarthy, C. 1999, *ApJ*, 512, L63
 Weidenschilling, S. J., & Cuzzi, J. N. 1983, *Protostars and Planets III*, ed. E. H. Levy & J. I. Lunine (Tucson: Univ. Arizona Press), 1031
 Weintraub, D. A., Sandell, G., & Duncan, W. D. 1989, *ApJ*, 340, L69
 Whitney, B. A., & Hartmann, L. 1992, *ApJ*, 395, 529
 Wichmann, R., Bastian, U., Krautter, J., Jankovics, I., & Rucinski, S. M. 1998, *MNRAS*, 301, L39
 Wilner, D. J., Ho, P. T. P., Kastner, J. H., & Rodríguez, L. F. 2000, *ApJ*, 534, L101
 Zuckerman, B., Forveille, T., & Kastner, J. H. 1995, *Nature*, 373, 494
 Zuckerman, B., Webb, R. A., Schwartz, M., & Becklin, E. E. 2001, *ApJ*, 549, L233